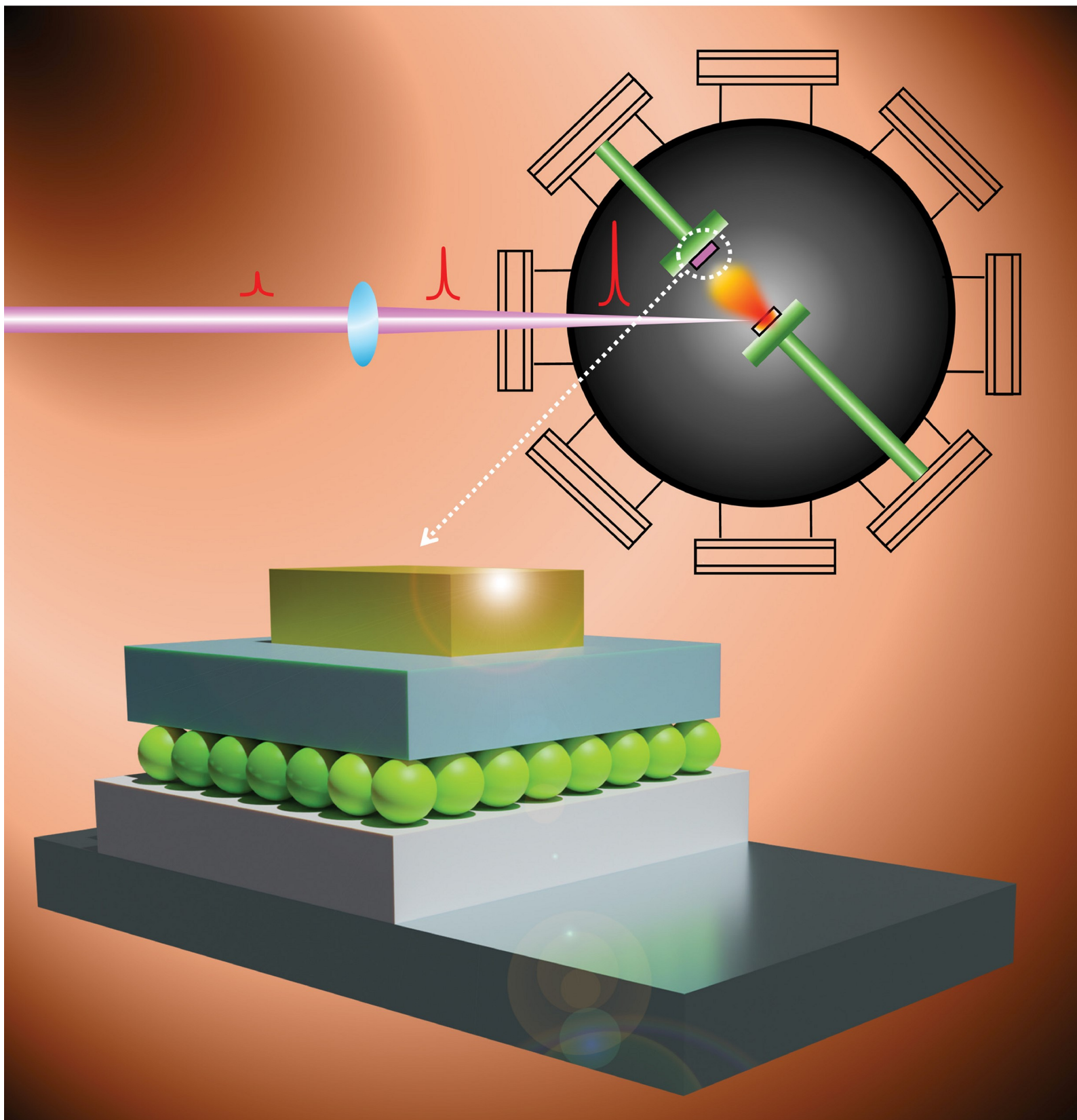


ACS **APPLIED**
ENERGY MATERIALS

June 23, 2025
Volume 8
Number 12
pubs.acs.org/acsaem



ACS Publications
Most Trusted. Most Cited. Most Read.

www.acs.org

Efficient Quantum Dot Solar Cells with Sustainable Oxide Thin Films

Amit Acharya, Mingxiao Ye, Jeff Kabel, Sambhawana Sharma, Anjana Asthana, Kumar Neupane, Join Uddin, Dongyan Zhang, and Yoke Khin Yap*

Cite This: *ACS Appl. Energy Mater.* 2025, 8, 8110–8116

Read Online

ACCESS |



Metrics & More



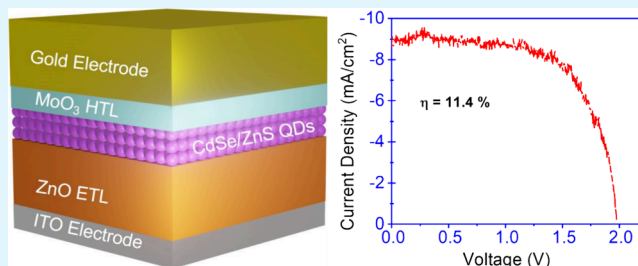
Article Recommendations



Supporting Information

ABSTRACT: Thin-film solar cells are more promising for low-cost and large-area photovoltaic devices. Tremendous efforts have been invested in using cadmium telluride (CdTe), copper indium gallium selenide (CIGS), and perovskite thin films for energy harvesting. In contrast, zinc oxide (ZnO) and molybdenum trioxides (MoO₃) are relatively earth-abundant, environmentally stable, and sustainable for thin-film solar cells. ZnO nanostructures have recently gained success in producing effective (~8.55%) quantum dot solar cells (QDSCs). While nanostructures offer high surface areas to receive electrons from quantum dots (QDs), they are dominated by surface dangling bonds. These defects can trap electrons and limit effective transport at the interface between the ZnO nanostructures and QDs. We anticipate that QDSCs based on thin-film materials can minimize such interface trapping states and be more efficient than those demonstrated with ZnO nanostructures. We strategically develop quality ZnO and MoO₃ thin films to produce QDSCs with power conversion efficiency as high as 11.4%. Our approach will inspire others to use scalable thin-film technology and QDs for solar energy harvesting based on sustainable ZnO and MoO₃.

KEYWORDS: quantum dot solar cells, solar cells, zinc oxide, molybdenum trioxide, pulsed-laser deposition



INTRODUCTION

Thin-film solar cells are well-recognized for their lightweight, low-cost, and flexible features. Thin films of silicon, cadmium telluride (CdTe), and copper indium gallium selenide (CIGS) are often used for such devices.^{1–3} More recently, perovskite^{4–10} and perovskite/CIGS tandem¹¹ are emerging as materials for efficient thin-film photovoltaic devices. Material stability issues have limited commercial use of perovskite solar cells (PSCs),¹² while CdTe and CIGS devices face difficulty in composition control and supply shortage of rare metals such as tellurium and indium.⁶ Conversely, ZnO and TiO₂ are relatively stable and earth-abundant compared to CdTe, CIGS, and perovskite. Most studies use ZnO and TiO₂ nanostructures as the electron transport layers (ETLs) for quantum dot solar cells (QDSCs)^{13–15} with exceptional power conversion efficiency (PCE) as high as ~8.55 and 12.98% by using ZnO¹⁶ and TiO₂¹⁷ nanostructures as the ETLs, respectively.

The surfaces of nanostructures are full of dangling bonds, which can trap electrons and limit effective charge transport at the interface of the nanostructures and the QD active layers. Therefore, we anticipate that QDSCs based on ZnO thin films can be more efficient than those demonstrated with ZnO nanostructures. Here, we present a thin-film technology strategy to produce efficient QDSCs with a PCE of 11.4%. Our best PCE is significantly higher than the reported work using ZnO nanostructures as the ETL in CdS/CdSe QDs cosensitized solar cells, where the best PCEs are around

3.45%¹⁸ to 4.68%.¹⁹ Our approach would inspire others to revisit using thin-film technology to make more efficient solar cells scalable in the device area and stable under ambient conditions.

RESULTS AND DISCUSSION

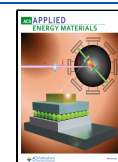
The device structure of this study and the corresponding energy diagram^{20,21} are shown in Figure 1. Figure 1a shows that light irradiation must pass through the ITO and ZnO films before reaching the CdSe/ZnS core-shell QDs active layer. Therefore, the ITO and ZnO films must be highly transparent to maximize photon irradiation of the QDs. Once electron-hole pairs are generated on the QDs, electrons must be effectively transported through the ZnO ETL to the ITO electrode, and holes must move through the molybdenum trioxide (MoO₃) hole transport layer (HTL) to the gold electrode to complete the current loop. As shown in Figure 1b, the layered structure of ITO/ZnO/QDs/MoO₃/Au is energetically favored for efficient electron-hole pair separation. First, electrons are generated on the CdSe core, tunnel

Received: February 28, 2025

Revised: May 23, 2025

Accepted: May 28, 2025

Published: June 10, 2025



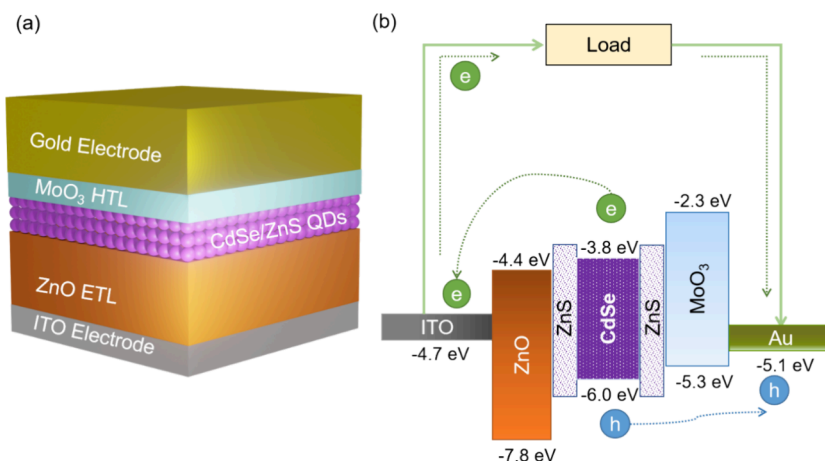


Figure 1. (a) Schematic diagram and (b) energy band diagram of the device.

through the ZnS shells, and are transported through the ZnO films before reaching the ITO electrode. Hole transport from CdSe to MoO₃/Au is also energetically favored, as shown in Figure 1b. The quality of ZnO, QDs, and MoO₃ must be enhanced to facilitate their optimum functions. Defective ZnO and MoO₃ induce charge recombination due to charge trapping at the defect points and the interfaces. In this work, all ZnO and MoO₃ thin films are deposited using the UV pulsed laser deposition (PLD) technique, schematically represented in Figure S1. Our strategy is to use a deep UV (266 nm), short-pulsed (~5 ns full width at half-maximum), and low pulsed-energy laser, proven to produce a fine and reactive laser plume for crystalline nano²² and atomic^{23,24} structures at room temperature (RT).

The properties of ZnO thin films at various stages of device fabrication are studied by field emission scanning electron microscopy (FESEM) imaging, UV–vis spectroscopy, and photoluminescence (PL) spectroscopy. Figure 2a shows the PL spectra of ZnO deposited on the Si substrates under

ambient O₂. A strong emission at ~390 nm is detected, which belongs to the near band edge emission (NBE) due to the recombination of free excitons in ZnO.^{25,26} Some reports detected a defective PL band at 420 nm, but our samples do not have it. Such defective PL bands are due to electron transitions from the shallow donor level of oxygen vacancies to the valence band or from the shallow donor level of Zn interstitials to the valence band.²⁷ Therefore, the predominant 390 nm emission detected here suggests the formation of quality ZnO films by our deep UV PLD approach. In contrast, we have deposited the ZnO film by PLD in a vacuum. The deposited films emit weak PL signals with significant defective signals at ~420 nm (Figure S2 and Supporting Information). This result suggests that our deep UV laser could produce an energetic laser plume that reacts with oxygen gas to form quality ZnO films with minimum oxygen vacancies, even at RT.

We studied the transmission of high-quality ZnO films deposited in ambient O₂. Figure 2b shows that the UV–vis transmittance spectrum displays an absorption peak at ~370 nm, consistent with the ZnO direct band gap of 3.37 eV. The average transmittance percentage in the visible light range is over 90%. The high transparency is associated with improved crystallinity and more stoichiometric films.²⁸ The inset of Figure 2b shows the smooth surface morphology of the ZnO films. High-quality ZnO films were also indicated by X-ray photoelectron and Auger spectroscopy data (Figure S3, eqs S1 and S2).

The optical transmission of ZnO coated on commercial ITO-coated glass is shown in Figure 2c. The ZnO-coated ITO glass is optically transparent (~90%) in the ~400–1000 nm wavelength range. After spin-coating the QDs on the ZnO, the transparency is higher than ~70%. This means the incoming solar radiation can reach the whole thickness of the QD active layer while being sufficiently absorbed to produce the electron–hole pairs. The QD suspension was coated to ~1" × 1" area for this controlled sample to ensure proper UV–vis measurement. After spin-coating the QDs on ZnO, the UV–vis plot shows a sharp absorption peak at 530 nm corresponding to that of the CdSe/ZnS core–shell structure.¹⁶ Such optical properties are retained after coating of the MoO₃ film (20 nm). This means that the MoO₃ films are optically transparent, which allows photons reflected from the gold electrode to pass through the QD active layer again to generate more electron–hole pairs.

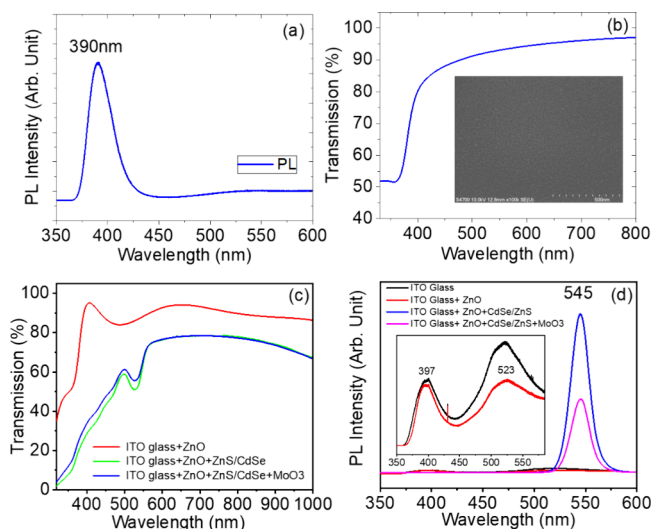


Figure 2. (a) Photoluminescence (PL) of an as-deposited ZnO thin film on a Si substrate at RT. (b) UV–vis transmission spectrum of a ZnO thin film coated on a quartz substrate. The inset shows the film morphology of ZnO coated on a Si substrate. (c) UV–vis transmittance spectra and (d) PL spectra of a QDSC device at different synthesis steps.

The PL spectra at various solar cell fabrication steps are shown in Figure 2d. The commercial ITO glass shows two PL peaks at 397 and 523 nm. Such PL spectra are retained after coating the ZnO film, suggesting that the PL of the ITO film dominates. After the QDs are coated, the PL spectrum shows the dominant peak at 545 nm, originating from the CdSe/ZnS QDs (540 ± 10 nm, according to the product specification). The PL intensity of the QDs becomes weaker after the deposition of the MoO₃ HTL, suggesting effective electron–hole separation.

We deposited the MoO₃ HTLs by PLD at RT in ambient O₂. We found that coating these HTL films at elevated temperatures leads to nanostructured porous films (see the Supporting Information and Figure S4) and causes device failure upon coating of gold electrodes. We are interested in depositing high-quality, electrically insulating MoO₃ films. Therefore, we decided to inspect the optical properties of MoO₃ films coated on quartz substrates at RT. Figure 3a shows that MoO₃ films coated in a vacuum have a low transmission of ~55–65%.

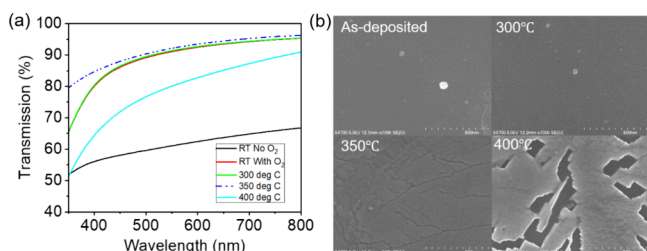


Figure 3. (a) UV–vis spectra of as-deposited MoO₃ films coated at RT in ambient O₂, and after annealing at various temperatures, as compared to that deposited at RT in vacuum. (b) Surface morphologies of as-deposited MoO₃ films coated at RT in ambient O₂ and after annealing at various temperatures.

In contrast, the transmission of MoO₃ films coated in ambient O₂ under the same PLD parameters is highly transparent. Interestingly, the transmission of MoO₃ films coated in ambient O₂ was retained after annealing at 300 °C, but it deteriorated after annealing at 400 °C. Although annealing up to ~350 °C retains the optical transparency of the MoO₃ films, such a process will cause texturing and cracking of the film morphology shown in Figure 3b. Therefore, we decided to use as-deposited HTLs at RT under ambient ambient O₂ for all QDSCs here. The XPS study also indicates that MoO₃ films coated in ambient O₂ are of higher quality (Supporting Information and Figure S5).

Next, we fabricated QDSCs based on the high-quality ZnO and MoO₃ films discussed. As shown in Figure 4a, we have constructed QDSCs with different thicknesses of ZnO thin films while keeping all other parameters (MoO₃ thickness ~20 nm, suspension of QDs volume ~300 μL) unchanged. The highest efficiency of 11.4% was obtained with the 80 nm thick ZnO film. The corresponding current density–voltage (*J*–*V*) curves are shown in Figure 4b. Table 1 summarizes the changes in open-circuit voltage (*V*_{OC}), current density (*J*_{SC}), power density (*P*_M), fill factor (FF), PCE, shunt resistance (*R*_{SH}), and series resistance (*R*_S) with the increase in ZnO thickness. As tabulated, all these parameters reach the maxima near ~80 nm. *R*_S, on the other hand, becomes lowest at ~80 nm. A low *R*_S and a high *R*_{SH} are desirable for efficient photovoltaic devices. Low *R*_S reduces the resistance of

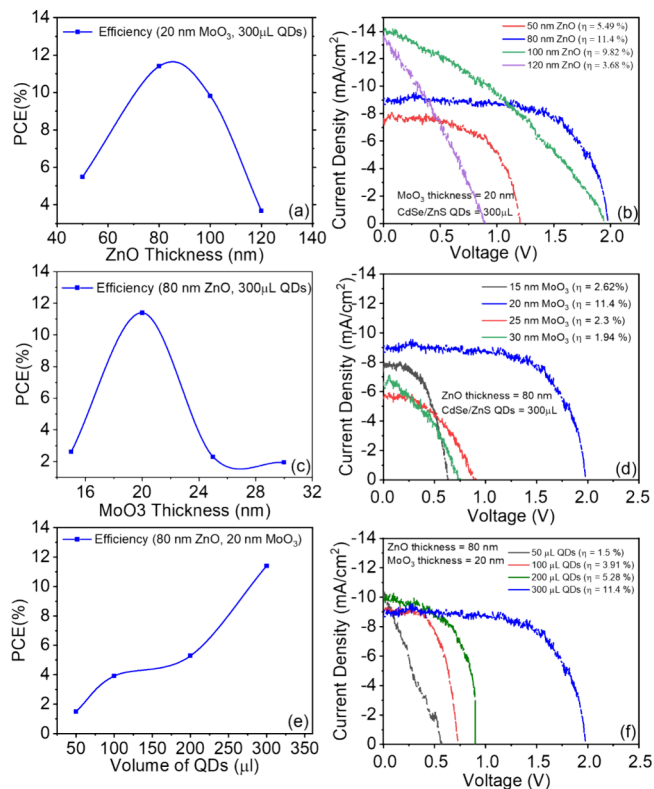


Figure 4. (a) Power conversion efficiency (PCE) and (b) current density–voltage (*J*–*V*) of solar cell devices at different ZnO thicknesses. (c) PCE and (d) *J*–*V* of solar cell devices at different MoO₃ thicknesses. (e) PCE and (f) *J*–*V* of solar cell devices at different volumes of QD suspension.

photocurrent and, therefore, increases the FF and PCE. On the other hand, high *R*_{SH} (parallel resistance to the solar cell) will minimize the alternate current path for the light-generated current. Therefore, higher *R*_{SH} values can reduce solar power loss. *R*_{SH} is highest at the optimum 80 nm thick ZnO, and enables maximum *V*_{OC} to promote charge transport across ETL and HTL.

On the other hand, *J*_{sc} is increasing with the ZnO film thickness. *J*_{sc} is the current density through the device at zero applied voltage directly depending on several factors, such as the amount of light effectively reaching the QDs to produce electron–hole pairs, the spectrum of the incident light, the solar cells’ optical properties, and the carrier collection probability. For SCs with the same material types and device size, all these factors are similar for all devices compared here, except the carrier collection probability. The possible explanation for the thicker ZnO being less defective is that the bulk of the films is far from the lattice-mismatched ITO–ZnO interface. The thicker ZnO would reduce carrier trapping, increase the collection probability, and, therefore, higher *J*_{sc}.

Next, we examine the effect of the HTL. MoO₃ is a member of transition metal oxides widely used as alternatives to poly(3,4-ethylenedioxythiophene): poly(styrenesulfonate) (PEDOT:PSS) as the HTL due to high hole mobility and good environmental stability. PEDOT:PSS compromises the device stability due to its hygroscopic nature and low work function metal degradation.^{18,19} We therefore analyzed MoO₃ thin films of different thicknesses deposited by PLD while keeping all other parameters constant (ZnO film thickness ~80 nm, suspension of QD volume ~300 μL).

Table 1. Summary of Key Parameters of Figure 4a,b^a

ZnO film thickness (nm)	V_{OC} (V)	J_{SC} (mA/cm ²)	P_M (mW/cm ²)	FF	PCE (%)	R_{SH} (Ω /cm ²)	R_S (Ω /cm ²)
50	1.20	7.61	5.49	0.60	5.49	696	49
80	1.98	9.00	11.40	0.67	11.40	1469	8
100	1.94	14.28	9.82	0.34	9.82	242	93
120	0.89	13.45	3.68	0.31	3.68	86	51

^aAll devices have constant MoO₃ thickness (20 nm) and QD volume (300 μ L).

Table 2. Summary of Key Parameters of Figure 4c,d^a

MoO ₃ film thickness (nm)	V_{OC} (V)	J_{SC} (mA/cm ²)	P_M (mW/cm ²)	FF	PCE (%)	R_{SH} (Ω /cm ²)	R_S (Ω /cm ²)
15	0.63	7.72	2.62	0.54	2.62	335	35
20	1.90	9.00	11.40	0.67	11.40	1469	8
25	0.90	5.62	2.30	0.46	2.30	2631	116
30	0.74	6.70	1.94	0.39	1.94	245	115

^aAll devices have a constant ZnO thickness (80 nm) and a QD volume of QDs (300 μ L).

Table 3. Summary of Key Parameters of Figure 4e,f^a

volume of QDs (μ L)	V_{OC} (V)	J_{SC} (mA/cm ²)	P_M (mW/cm ²)	FF	PCE (%)	R_{SH} (Ω /cm ²)	R_S (Ω /cm ²)
50	0.56	10.33	1.51	0.26	1.51	52	66
100	0.73	9.08	3.91	0.59	3.91	1069	25
200	0.90	10.00	5.29	0.58	5.28	401	22
300	1.90	9.00	11.40	0.67	11.40	1469	8

^aAll devices have a constant MoO₃ thickness (20 nm) and ZnO thickness (80 nm).

Figure 4c shows that the favorable MoO₃ thickness for the optimized device performance was 20 nm. Figure 4d shows that the device with the highest efficiency (PCE = 11.4%) is associated with a higher fill factor (FF = 0.67) and current density ($J_{SC} = 9.0$ mA cm⁻²), which suggests the 20 nm thick MoO₃ is highly hole conductive (electron resistive) with relatively low R_S . MoO₃ of similar film thickness resulted in the best working devices, as reported by others.²⁹ MoO₃ films thinner than 20 nm are more defective due to mechanical stress introduced by the two interfaces between QDs/MoO₃ and MoO₃/Au. Therefore, thinning the film increases the probability of high leakage current, which could not function as an HTL, resulting in worse device reproducibility. Thicker MoO₃ films likely deteriorated the device's performance due to increased hole transport series resistance (R_S). Table 2 summarizes the changes of V_{OC} , J_{SC} , P_M , FF, PCE, R_{SH} , and R_S with an increased MoO₃ thickness. The device with the highest PCE also corresponds with the highest V_{OC} , J_{SC} , P_M , FF, PCE, and the lowest R_S , signifying that 20 nm MoO₃ film is optimum for the potential buildup to maximize photocurrent and yet less resistive for hole transport.

Besides the charge transport effects within the ETL and HTL, the PCEs of QDSCs rely on exciton production. Therefore, we have prepared a series of devices with different volumes of the QD suspension (i.e., different thicknesses of the QD films) while keeping other optimized parameters unchanged (ZnO film thickness \sim 80 nm, MoO₃ film thickness \sim 20 nm). Figure 4e,f show that PCE and V_{OC} increase with the amount of QDs coated in the suspension. The bandgap of the QDs decides the upper limit of V_{OC} .³⁰ However, within the upper limit, several factors can change V_{OC} , including the device temperature,³¹ light intensities,³² carrier concentration,^{33,34} and recombination kinetics.^{33–35} The increased volume of QD suspension used will affect only the carrier concentration and recombination kinetics. Using more QDs in the active layer generates more electron–hole pairs. This will

increase the carrier concentration and enhance the built-in potential when the enhancement overcomes the recombination and produces excess charges.^{33,34} This is consistent with the increase in V_{OC} that we observed as the volume of QDs used increases (Figure 4f), corresponding to the increases in the built-in field across the gold and ITO electrodes that drive the charge transport across the ETL and HTL. We observed a maximum PCE when we coated 300 μ L of QDs. Data with 350 μ L are not reproducible and are not shown here. As we further increased QDs to 350 μ L, the diffusion of electrons and holes toward the ETL and HTL became more resistive at the thicker QD layer and generally decreased the PCE.

Table 3 summarizes the changes of V_{OC} , J_{SC} , P_M , FF, and PCE with the increase of the QD suspension volume. As discussed, the V_{OC} increases with the applied volume of QDs, contributing to the increase in PCE. J_{SC} is relatively constant for all cases as the optical properties of other coatings (ITO, ZnO, MoO₃, and gold) are identical. R_{SH} and FF are also highest for 300 μ L of QD suspension. R_S is lowest for devices with 300 μ L of QDs, consistent with the high PCE.

We further study the reason for a peak PCE at a ZnO film thickness of 80 nm. Figure 5a shows that the transmission of ZnO films on ITO glasses is quite similar around the wavelength range of \sim 450–650 nm (peak solar intensity range), maybe slightly lower in transmission for 40 and 60 nm ZnO films. This means that ZnO films cause similar optical loss at various thicknesses and affect the internal quantum yield equally. We further studied the current–voltage (I – V) characteristics of ZnO films through the film thickness. We coat these films on copper (Cu, 99.9%) substrates for better electrical contacts. Figure 5b shows that the thinner ZnO films (40 and 60 nm) are metallic. In contrast, the 100 and 120 nm films are electrically insulating and overlap near zero. The behaviors of the 80 nm film is in-between those of the thinner and thicker films. The 80 nm film is more semiconducting-like, which allows it to hold a higher built-in potential to enable

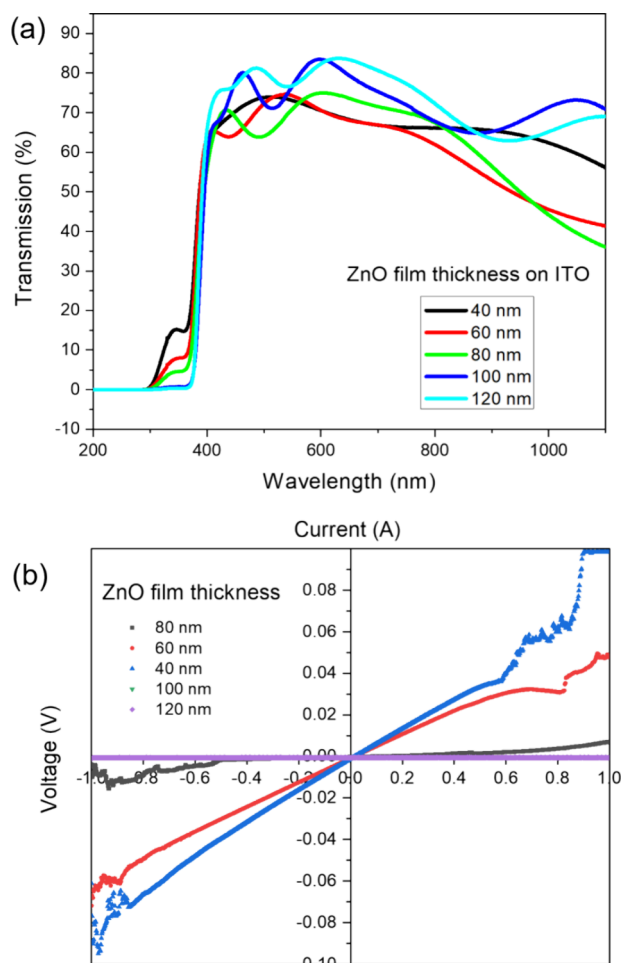


Figure 5. (a) UV-vis transmission spectra and (b) I - V characteristics of ZnO films at various thicknesses.

higher V_{oc} for effective electron-hole pair separation and lead to higher FF and PCE as shown in Figure 4.

We propose a mechanism to explain a peak PCE with an optimum ZnO film thickness of 80 nm. It is well accepted that the defect density in thin films is higher near the film/substrate interface. The higher defect density is due to the lattice mismatch between the film and the substrate and interface stress due to thermal expansion mismatch. This phenomenon was reported for thin films, including ZnO films coated on a -plane sapphire substrates.³⁶ For our case, we believe that thicker ZnO (80 nm) would offer fewer defects and better semiconducting properties in comparison to the thinner films. The thicker 100 and 120 nm films become nonconductive, likely due to carrier trapping at longer transport lengths. Therefore, the PCE dropped after the peak at 80 nm, as shown in Figure 4a.

The structural characterization of the ZnS/CdSe core-shell QD samples was carried out using an aberration-corrected scanning transmission electron microscope (STEM/TEM, FEI Titan Themis 200 kV), operated at 200 kV. Figure 6a,b are the low-magnification bright-field images showing the shape and size distribution of the CdSe QDs. The TEM image shows that the average diameter of the CdSe QDs varies from 7 to 10 nm. The inset shows the corresponding diffraction pattern of the CdSe QDs. The electron diffraction patterns confirm the wurtzite hexagonal structure of this sample as all the powder

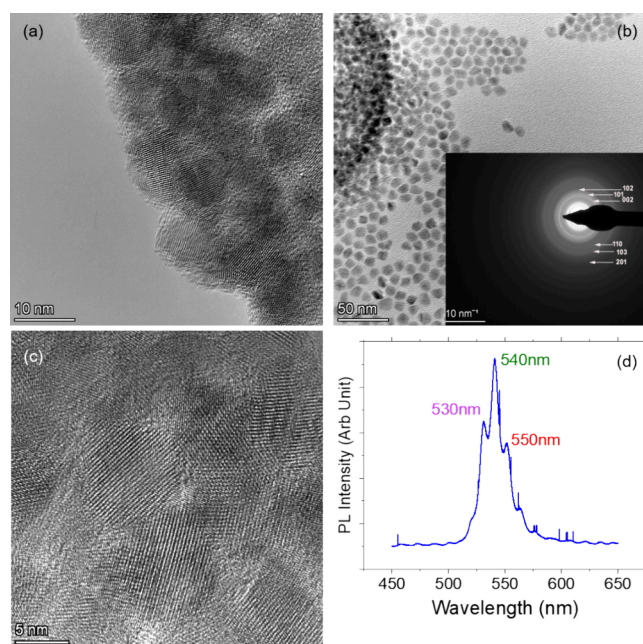


Figure 6. TEM images of CdSe/ZnS core-shell CdSe/ZnS QDs (a–c) and the electron diffraction patterns (inset). (d) PL spectra of the QDs.

diffraction rings could be indexed using a hexagonal structure: $a = 4.299 \text{ \AA}$, $c = 7.010 \text{ \AA}$, and $P63mc$. The CdSe nanocrystals exhibited a single crystalline nature, as evident from the high-resolution lattice images in Figure 6c. Figure 6d shows the PL spectra of the QDs coated on a quartz substrate. There are at least three major luminescence peaks around 530, 540, and 550 nm, consistent with the product specification ($540 \pm 10 \text{ nm}$). These PL peaks suggest the optical bandgaps of 2.25–2.34 eV.

CONCLUSIONS

We demonstrated that high-quality ZnO ETL, MoO_3 HTL, and QDs with optimum coating thicknesses could lead to highly efficient QDSCs based on a thin-film technology. We believe that the interfaces between ZnO and QDs and between MoO_3 and QDs play essential roles in maximizing J_{sc} and V_{oc} , which are the keys to high PCE. High-quality, low-defect films and interfaces are vital to minimize carrier trapping and maximize PCE. This work will inspire more efforts to produce solar cells with abundant materials based on thin-film technology using a spectrum of other materials systems.

EXPERIMENTAL SECTION

Materials. CdSe/ZnS core-shell quantum dots suspended in toluene (12.5 mg/mL) were purchased from Mesolight (Suzhou Xingshuo Nanotech Co.). The commercial ITO-coated glass was purchased from Delta Technologies. The 99.9% pure ZnO target and the 99.99% pure MoO_3 target were purchased from Kurt J. Lesker. The gold (99.99% purity) PLD target was purchased from Kurt Lesker Company. Reagent-grade acetone and isopropyl alcohol were purchased from Sigma-Aldrich.

Device Fabrication and Characterization. The commercial ITO thin film-coated glass was cleaned with acetone, then with isopropyl alcohol (IPA), and deionized (DI) water by sonicating for 5 min each. The sample was dried with a nitrogen gas gun and placed on a PLD substrate holder. The ZnO target was placed following the schematic diagram for the PLD setup shown in Figure S1. High-quality ZnO thin films were grown on commercial ITO glass substrates at RT using a fourth harmonic generation (4ω) of a Q-

switched Nd: YAG pulsed-laser at 10 Hz with an output wavelength of 266 nm focused on a ZnO target surface using a quartz lens. The deposition chamber was first evacuated to a base pressure of about 5×10^{-5} mbar and oxygen gas was admitted under an optimized delivery pressure of 50 mTorr (6.67×10^{-2} mbar) to get the highest quality thin films. The time of ablation of the ZnO target and the deposition thickness are monitored using a thickness monitor. The laser beam was then focused to a laser spot (~ 1 mm in diameter) and was scanned over the ZnO target by an x - y motorized mirror. The power of the laser was estimated to be 25 mJ/pulse. The target was rotated to achieve a uniform thickness distribution of the ZnO thin films.

After the deposition of ZnO thin films on commercial ITO glass, CdSe/ZnS core-shell quantum dots were spin-coated layer by layer on top of planar ZnO films. For this process, two drops (~ 10 μ L each) of CdSe/ZnS QD solution (12.5 mg/mL in Toluene) were dropped on the substrate and left to semidry. The substrate was spun for 1 min at 2500 rpm. This process was repeated after the film was completely dry until the targeted QD volume was used. 300 μ L QDs were used for the best efficiency to get a uniform layer. These QDs are then overcoated with an MoO₃ thin film at RT with the same PLD setup and procedures described earlier for ZnO coating. We found that the PLD coating step is sufficient to remove the ligands from the QD surfaces. The local heating from the laser plasma and the bombardment of the energetic laser plume likely work as the stripping process. A 100 nm Au anode was finally deposited on the MoO₃ hole transport layer (HTL) by PLD through a shadow mask at a 2 nm/min rate within a 10^{-5} mbar base pressure. The active device area is defined by the overlap of the Au anode with the ITO cathode and is determined to be 10 mm². Current and voltage (I - V) measurements were performed using a computer-controlled Keithley 2636A source meter under the illumination of a solar simulator (125 W Newport 96000 xenon arc lamp equipped with an AM 1.5G filter) at an intensity of 100 mW/cm² (1 Sun illumination). It is to be noted that the data shown here are those with the highest PCEs out of the two-five devices we made under the same parameters. The PCE standard deviation among the working devices is about 30%. The deviation for the V_{OC} and J_{SC} is about 15–18%. Such a deviation is likely due to the variation in the uniformity and coverage of spin-coated QDs, which is relatively less controllable. We observed that these devices performed better after a few cycles of I - V sweeps, likely due to the solar soaking effects.^{37,38} Depending on the type of solar cells, there are various hypotheses for such improvement,^{37–39} but generally, solar soaking improves charge transport due to reduced defects. Devices are stable until unexpected short circuits occur at high bias voltages.

Scanning electron microscopy imaging was conducted with a Hitachi S-4700 FE-SEM. Photoluminescence spectra were measured at RT with a He-Ne laser at a wavelength of 325 nm by a Jobin-Yvon LabRAM HR800 Raman Spectrometer. Optical transmittance was measured with a UV-vis spectrophotometer. X-ray photoelectron spectroscopy measurements were performed with a PHI 5800 X-ray photoelectron spectrometer with a source anode of Mg ($h\nu = 1253.6$ eV).

■ ASSOCIATED CONTENT

SI Supporting Information

The Supporting Information is available free of charge at <https://pubs.acs.org/doi/10.1021/acsaem.5c00612>.

Additional experimental details, experimental setup, and supporting data (PDF)

■ AUTHOR INFORMATION

Corresponding Author

Yoke Khin Yap – Department of Physics, and The Elizabeth and Richard Henes Center for Quantum Phenomena, Michigan Technological University, Houghton, Michigan

49931, United States; orcid.org/0000-0002-1224-4120;
Email: ykyap@mtu.edu

Authors

Amit Acharya – Department of Physics, and The Elizabeth and Richard Henes Center for Quantum Phenomena, Michigan Technological University, Houghton, Michigan 49931, United States

Mingxiao Ye – Department of Physics, and The Elizabeth and Richard Henes Center for Quantum Phenomena, Michigan Technological University, Houghton, Michigan 49931, United States

Jeff Kabel – Department of Physics, and The Elizabeth and Richard Henes Center for Quantum Phenomena, Michigan Technological University, Houghton, Michigan 49931, United States

Sambhawana Sharma – Department of Physics, and The Elizabeth and Richard Henes Center for Quantum Phenomena, Michigan Technological University, Houghton, Michigan 49931, United States

Anjana Asthana – Department of Materials Science and Engineering, Michigan Technological University, Houghton, Michigan 49931, United States

Kumar Neupane – Department of Physics, and The Elizabeth and Richard Henes Center for Quantum Phenomena, Michigan Technological University, Houghton, Michigan 49931, United States; orcid.org/0009-0005-4042-6481

Join Uddin – Department of Physics, and The Elizabeth and Richard Henes Center for Quantum Phenomena, Michigan Technological University, Houghton, Michigan 49931, United States

Dongyan Zhang – Department of Physics, and The Elizabeth and Richard Henes Center for Quantum Phenomena, Michigan Technological University, Houghton, Michigan 49931, United States

Complete contact information is available at:
<https://pubs.acs.org/doi/10.1021/acsaem.5c00612>

Author Contributions

The manuscript was written with contributions from all authors. All authors have approved the final version of the manuscript.

Notes

The authors declare no competing financial interest.

■ ACKNOWLEDGMENTS

The authors gratefully acknowledge the financial support from the Elizabeth and Richard Henes Center for Quantum Phenomena and the Jim '66 and Shelley Williams Applied Physics Annual Fund.

■ REFERENCES

- (1) Lee, T. D.; Ebong, A. U. A review of thin film solar cell technologies and challenges. *Renewable and Sustainable Energy Reviews* **2017**, *70*, 1286–1297.
- (2) Keller, J.; Kiselman, K.; Donzel-Gargand, O.; Martin, N. M.; Babucci, M.; Lundberg, O.; Wallin, E.; Stolt, L.; Edoff, M. High-concentration silver alloying and steep back-contact gallium grading enabling copper indium gallium selenide solar cell with 23.6% efficiency. *Nature. Energy* **2024**, *9* (4), 467–478.
- (3) Scarpulla, M. A.; McCandless, B.; Phillips, A. B.; Yan, Y.; Heben, M. J.; Wolden, C.; Xiong, G.; Metzger, W. K.; Mao, D.; Krasikov, D.; et al. CdTe-based thin film photovoltaics: Recent advances, current

challenges and future prospects. *Sol. Energy Mater. Sol. Cells* **2023**, *255*, No. 112289.

(4) Yang, W. S.; Noh, J. H.; Jeon, N. J.; Kim, Y. C.; Ryu, S.; Seo, J.; Seok, S. I. High-performance photovoltaic perovskite layers fabricated through intramolecular exchange. *Science* **2015**, *348* (6240), 1234–1237.

(5) Jeon, N. J.; Noh, J. H.; Yang, W. S.; Kim, Y. C.; Ryu, S.; Seo, J.; Seok, S. I. Compositional engineering of perovskite materials for high-performance solar cells. *Nature* **2015**, *517* (7535), 476.

(6) Ramanujam, J.; Singh, U. P. Copper indium gallium selenide based solar cells—a review. *Energy Environ. Sci.* **2017**, *10* (6), 1306–1319.

(7) Lin, R.; Xiao, K.; Qin, Z.; Han, Q.; Zhang, C.; Wei, M.; Saidaminov, M. I.; Gao, Y.; Xu, J.; Xiao, M.; et al. Monolithic all-perovskite tandem solar cells with 24.8% efficiency exploiting comproportionation to suppress Sn(II) oxidation in precursor ink. *Nature Energy* **2019**, *4* (10), 864–873.

(8) Matsui, T.; Yamamoto, T.; Nishihara, T.; Morisawa, R.; Yokoyama, T.; Sekiguchi, T.; Negami, T. Compositional Engineering for Thermally Stable, Highly Efficient Perovskite Solar Cells Exceeding 20% Power Conversion Efficiency with 85 °C/85% 1000 h Stability. *Adv. Mater.* **2019**, *31* (10), No. 1806823.

(9) Han, J.; Park, K.; Tan, S.; Vaynzof, Y.; Xue, J.; Diau, E. W.-G.; Bawendi, M. G.; Lee, J.-W.; Jeon, I. Perovskite solar cells. *Nature Reviews Methods Primers* **2025**, *5* (1), 3.

(10) Kim, J. Y.; Lee, J.-W.; Jung, H. S.; Shin, H.; Park, N.-G. High-Efficiency Perovskite Solar Cells. *Chem. Rev.* **2020**, *120* (15), 7867–7918.

(11) Han, Q. F.; Hsieh, Y. T.; Meng, L.; Wu, J. L.; Sun, P. Y.; Yao, E. P.; Chang, S. Y.; Bae, S. H.; Kato, T.; Bermudez, V.; et al. High-performance perovskite/Cu(In,Ga)Se-2 monolithic tandem solar cells. *Science* **2018**, *361* (6405), 904.

(12) Extance, A. The reality behind solar power's next star material. *Nature* **2019**, *570*, 429–432.

(13) Pan, Z.; Rao, H.; Mora-Seró, I.; Bisquert, J.; Zhong, X. Quantum dot-sensitized solar cells. *Chem. Soc. Rev.* **2018**, *47* (20), 7659–7702.

(14) Chebrolov, V. T.; Kim, H.-J. Recent progress in quantum dot sensitized solar cells: an inclusive review of photoanode, sensitizer, electrolyte, and the counter electrode. *Journal of Materials Chemistry C* **2019**, *7* (17), 4911–4933.

(15) Concina, I.; Vomiero, A. Metal Oxide Semiconductors for Dye- and Quantum-Dot-Sensitized Solar Cells. *Small* **2015**, *11* (15), 1744–1774.

(16) Chuang, C.-H. M.; Brown, P. R.; Bulović, V.; Bawendi, M. G. Improved performance and stability in quantum dot solar cells through band alignment engineering. *Nat. Mater.* **2014**, *13* (8), 796–801.

(17) Pan, Z.; Yue, L.; Rao, H.; Zhang, J.; Zhong, X.; Zhu, Z.; Jen, A. K. Y. Boosting the Performance of Environmentally Friendly Quantum Dot-Sensitized Solar Cells over 13% Efficiency by Dual Sensitizers with Cascade Energy Structure. *Adv. Mater.* **2019**, *31* (49), 1903696.

(18) Luo, J.; Sun, J.; Guo, P. C.; Yang, Z. S.; Wang, Y. X.; Zhang, Q. F. Enhancement in efficiency of CdS/CdSe quantum dots-sensitized solar cells based on ZnO nanostructures by introduction of MnS layer. *Mater. Lett.* **2018**, *215*, 176–178.

(19) Tian, J.; Zhang, Q.; Uchaker, E.; Gao, R.; Qu, X.; Zhang, S.; Cao, G. Architected ZnO photoelectrode for high efficiency quantum dot sensitized solar cells. *Energy Environ. Sci.* **2013**, *6* (12), 3542–3547.

(20) Das, S.; Alford, T. L. Optimization of the zinc oxide electron transport layer in P3HT:PC61BM based organic solar cells by annealing and yttrium doping. *RSC Adv.* **2015**, *5* (57), 45586–45591.

(21) Tvrdy, K.; Frantsuzov, P. A.; Kamat, P. V. Photoinduced electron transfer from semiconductor quantum dots to metal oxide nanoparticles. *Proc. Natl. Acad. Sci. U. S. A.* **2011**, *108* (1), 29–34.

(22) Lee, C. H.; Qin, S.; Savaikar, M. A.; Wang, J.; Hao, B.; Zhang, D.; Banyai, D.; Jaszczak, J. A.; Clark, K. W.; Idrobo, J.-C.; et al. Room-

Temperature Tunneling Behavior of Boron Nitride Nanotubes Functionalized with Gold Quantum Dots. *Adv. Mater.* **2013**, *25* (33), 4544–4548.

(23) Wang, J.; Kayastha, V. K.; Yap, Y. K.; Fan, Z.; Lu, J. G.; Pan, Z.; Ivanov, I. N.; Puzos, A. A.; Geohegan, D. B. Low Temperature Growth of Boron Nitride Nanotubes on Substrates. *Nano Lett.* **2005**, *5* (12), 2528–2532.

(24) Bhandari, S.; Hao, B.; Waters, K.; Lee, C. H.; Idrobo, J.-C.; Zhang, D.; Pandey, R.; Yap, Y. K. Two-Dimensional Gold Quantum Dots with Tunable Bandgaps. *ACS Nano* **2019**, *13* (4), 4347–4353.

(25) Bagnall, D. M.; Chen, Y. F.; Zhu, Z.; Yao, T.; Shen, M. Y.; Goto, T. High temperature excitonic stimulated emission from ZnO epitaxial layers. *Appl. Phys. Lett.* **1998**, *73* (8), 1038–1040.

(26) Bae, S. H.; Lee, S. Y.; Kim, H. Y.; Im, S. Effects of post-annealing treatment on the light emission properties of ZnO thin films on Si. *Opt. Mater.* **2001**, *17* (1–2), 327–330.

(27) Zhang, D. H.; Wang, Q. P.; Xue, Z. Y. Photoluminescence of ZnO films excited with light of different wavelength. *Appl. Surf. Sci.* **2003**, *207* (1–4), 20–25.

(28) Fortunato, E. M. C.; Barquinha, P. M. C.; Pimentel, A. C. M. B. G.; Gonçalves, A. M. F.; Marques, A. J. S.; Pereira, L. M. N.; Martins, R. F. P. Fully Transparent ZnO Thin-Film Transistor Produced at Room Temperature. *Adv. Mater.* **2005**, *17* (5), 590–594.

(29) Liu, R.; Lee, S.-T.; Sun, B. 13.8% Efficiency Hybrid Si/Organic Heterojunction Solar Cells with MoO₃ Film as Antireflection and Inversion Induced Layer. *Adv. Mater.* **2014**, *26* (34), 6007–6012.

(30) Rühle, S. Tabulated values of the Shockley–Queisser limit for single junction solar cells. *Sol. Energy* **2016**, *130*, 139–147.

(31) Nishioka, K.; Takamoto, T.; Agui, T.; Kaneiwa, M.; Uraoka, Y.; Fuyuki, T. Annual output estimation of concentrator photovoltaic systems using high-efficiency InGaP/InGaAs/Ge triple-junction solar cells based on experimental solar cell's characteristics and field-test meteorological data. *Sol. Energy Mater. Sol. Cells* **2006**, *90* (1), 57–67.

(32) Pepa, P. E.; Afungchui, D.; Holtomo, O.; Ebohenow, J. Parameters critically affecting the open circuit voltage of an organic solar cell. *Heliyon* **2025**, *11* (4), No. e42684.

(33) Sinton, R. A.; Cuevas, A. Contactless determination of current–voltage characteristics and minority-carrier lifetimes in semiconductors from quasi-steady-state photoconductance data. *Appl. Phys. Lett.* **1996**, *69* (17), 2510–2512.

(34) Väinölä, H.; Storgårds, J.; Yli-Koski, M.; Sinkkonen, J. Light induced change on the built-in potential of p/p+ structures and its effect on carrier lifetime measurements. *Materials Science and Engineering: B* **2002**, *91–92*, 421–424.

(35) Zhu, C.; Wang, C.; Zhang, P.; Ma, S.; Chen, Y.; Zhang, Y.; Yang, N.; Xiao, M.; Cheng, X.; Gao, Z.; et al. Topochemical assembly minimizes lattice heterogeneity in polycrystalline halide perovskites. *Joule* **2023**, *7* (10), 2361–2375.

(36) Saito, T.; Kato, A.; Yasui, K. Defect distribution in ZnO thin films grown on a-plane sapphire substrates by catalytic-reaction-assisted chemical vapor deposition. *J. Cryst. Growth* **2021**, *570*, No. 126206.

(37) Gostein, M.; Dunn, L. Light soaking effects on photovoltaic modules: Overview and literature review. In *2011 37th IEEE Photovoltaic Specialists Conference, 19–24 June 2011*; IEEE: 2011; pp 003126–003131.

(38) Jamarkattel, M. K.; Mathew, X.; Phillips, A. B.; Bastola, E.; Subedi, K. K.; Alifadhili, F. K.; Abudulimu, A.; Friedl, J. D.; Awni, R. A.; Li, D.-B.; et al. Reduced Recombination and Improved Performance of CdSe/CdTe Solar Cells due to Cu Migration Induced by Light Soaking. *ACS Appl. Mater. Interfaces* **2022**, *14* (17), 19644–19651.

(39) Gollino, L.; Zheng, D.; Mercier, N.; Pauporté, T. Unveiling of a puzzling dual ionic migration in lead- and iodide-deficient halide perovskites (d-HPs) and its impact on solar cell J–V curve hysteresis. *Exploration* **2024**, *4* (1), 20220156.